Cell Reports
Medicine

Article

Single-cell spatial transcriptomics reveals tumor microenvironment heterogeneity in primary and lymph node-metastatic small cell lung cancer

Graphical abstract

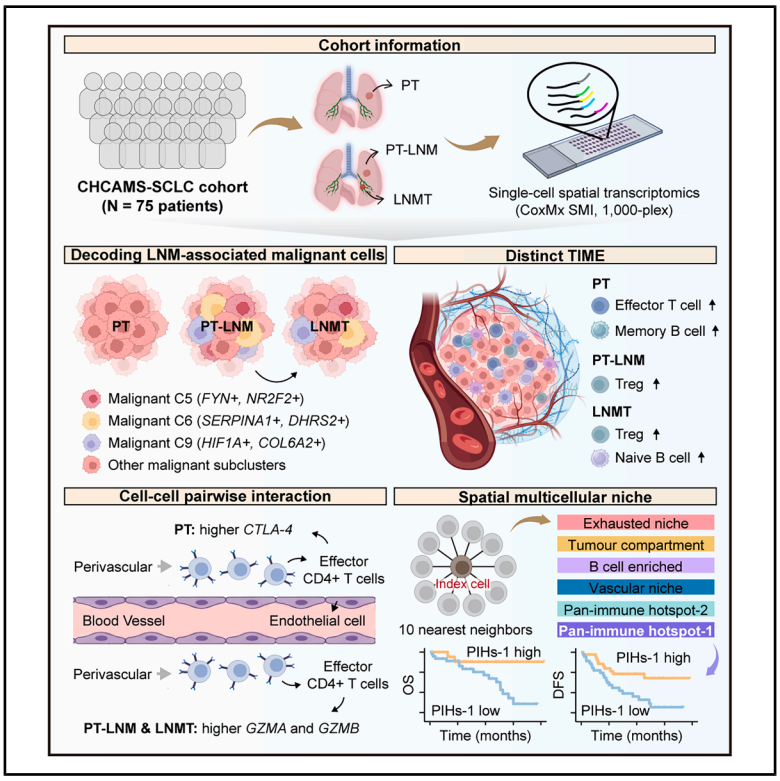

Highlights

- Single-cell spatial transcriptomics atlas of SCLC primary and lymph node metastasis
- LNM-enriched malignant states show immune exclusion and metabolic-angiogenic programs
- Vascular-immune crosstalk is spatially reprogrammed during lymph node metastasis
- PIHs-1 abundance independently predicts survival and defines a prognostic signature

Authors

Zicheng Zhang, Dongfang Wu, Ruanqi Chen, ..., Jianming Ying, Lin Yang, Meng Zhou

Correspondence

jmying@cicams.ac.cn (J.Y.),
yanglin@cicams.ac.cn (L.Y.),
zhoumeng@wmu.edu.cn (M.Z.)

In brief

Zhang et al. map the spatial landscape of primary and lymph node metastatic SCLC using single-cell spatial transcriptomics. They identify metastasis-enriched malignant subclusters, dynamic vascular-immune crosstalk, and a prognostic pan-immune hotspot. This spatially resolved atlas establishes lymph node-adaptive architectures as mechanistic correlates and translatable biomarkers for therapeutic discovery.

Zhang et al., 2026, Cell Reports Medicine 7, 102713
April 21, 2026
https://doi.org/10.1016/j.xcrm.2026.102713

CellPress

Cell Reports Medicine

CellPress
OPEN ACCESS

Article

Single-cell spatial transcriptomics reveals tumor microenvironment heterogeneity in primary and lymph node-metastatic small cell lung cancer

Zicheng Zhang,[1,2,6] Dongfang Wu,[3,6] Ruanqi Chen,[1] Modi Zhai,[2] Fan Yang,[1] Jiaqian Wang,[4] Lei Guo,[1] Li Liu,[1] Jianming Ying,[1,5,*] Lin Yang,[1,5,7,*] and Meng Zhou[2,*]

[1]Department of Pathology, National Cancer Center/National Clinical Research Center for Cancer/Cancer Hospital, Chinese Academy of Medical Sciences and Peking Union Medical College, Beijing 100021, P.R. China
[2]Institute of Genomic Medicine, School of Biomedical Engineering, Wenzhou Medical University, Wenzhou 325027, P.R. China
[3]MOE Key Laboratory of Gene Function and Regulation, School of Life Sciences, Sun Yat-sen University, Guangzhou 510275, China
[4]JMDNA Bio-Medical Technology Co., Ltd., Shanghai, China
[5]Beijing Key Laboratory of Multimodal Intelligent Diagnosis and Treatment for Tumors, Beijing 100021, P.R. China
[6]These authors contributed equally
[7]Lead contact
*Correspondence: jmying@cicams.ac.cn (J.Y.), yanglin@cicams.ac.cn (L.Y.), zhoumeng@wmu.edu.cn (M.Z.)
https://doi.org/10.1016/j.xcrm.2026.102713

SUMMARY

Lymph node metastasis (LNM) is a critical prognostic and therapeutic determinant in small cell lung cancer (SCLC), yet its spatial cellular ecosystem remains poorly understood. Here, we perform single-cell spatial transcriptomics using the CosMx Spatial Molecular Imager on 105 primary and metastatic lymph node specimens from 75 SCLC patients, generating a comprehensive atlas of over 600,000 cells. We identify three LNM-enriched malignant subclusters with distinct metabolic and angiogenic programs that spatially correlate with immune exclusion features. Spatial analysis reveals vascular-immune crosstalk, wherein endothelial cells orchestrate immune activation through avoidance of malignant cells while forming functional perivascular niches with cytotoxic T cells during LNM. Cellular neighborhood analysis delineates distinct multicellular niches and identifies a pan-immune hotspot (PIHs-1) whose abundance is an independent predictor of survival. This study provides a high-resolution spatial map of the SCLC tumor microenvironment during LNM and establishes spatially defined architectures as both mechanistic insights and translatable biomarkers.

INTRODUCTION

Small cell lung cancer (SCLC) is a highly aggressive neuroendocrine malignancy that accounts for about 15% of lung cancer cases and is characterized by rapid metastasis and poor prognosis.[1] The majority of SCLC patients already have metastatic disease at diagnosis, with lymph nodes (LNs), brain, liver, and bone being common sites of dissemination.[2] Despite initial responsiveness to chemotherapy and radiation, the prognosis for SCLC patients remains poor due to the high frequency of metastasis, recurrence, and treatment resistance.[3] Therefore, a better understanding of the molecular and cellular mechanisms underlying SCLC progression and metastasis is important for improving patient outcomes and developing more effective therapeutic interventions.

The metastatic potential of SCLC is attributed to its significant intra-tumoral heterogeneity, which may enable subpopulations of tumor cells to adapt to different microenvironments and evade immune surveillance.[4] Bulk and single-cell transcriptomic studies have revealed distinct molecular and cellular features associated with metastatic capacity, including transcriptional plasticity[5] and immune microenvironment remodeling.[6] However, these approaches, by necessitating tissue dissociation, do not capture the spatial organization of cells within the tumor microenvironment (TME), which is critical for understanding how cellular interactions influence tumor behavior. Recent advances in spatially resolved transcriptomics, such as Stereo-seq, Visium HD, GeoMx Digital Spatial Profiler, and CosMx Spatial Molecular Imager (SMI), allow for the mapping of cellular ecosystems within tumor tissues at the single-cell and subcellular resolutions and have revolutionized our understanding of the TME in cancers.[7–9] These technologies have begun to elucidate how the spatial arrangement of immune, stromal, and malignant cells influences progression and treatment efficacy in cancers such as esophageal squamous cell carcinoma,[10] melanoma,[11] non-SCLC,[12] ovarian cancer,[13] and pancreatic cancer.[14] Recent pioneering studies have provided novel insights into the spatial architecture of primary SCLC tumors, identifying features such as immune cell niches and neuroendocrine heterogeneity.[15–22] LNs are not passive receptacles but immunologically specialized organs that constitute a pivotal niche in the metastatic cascade. A systematic, high-resolution comparative analysis of the spatial

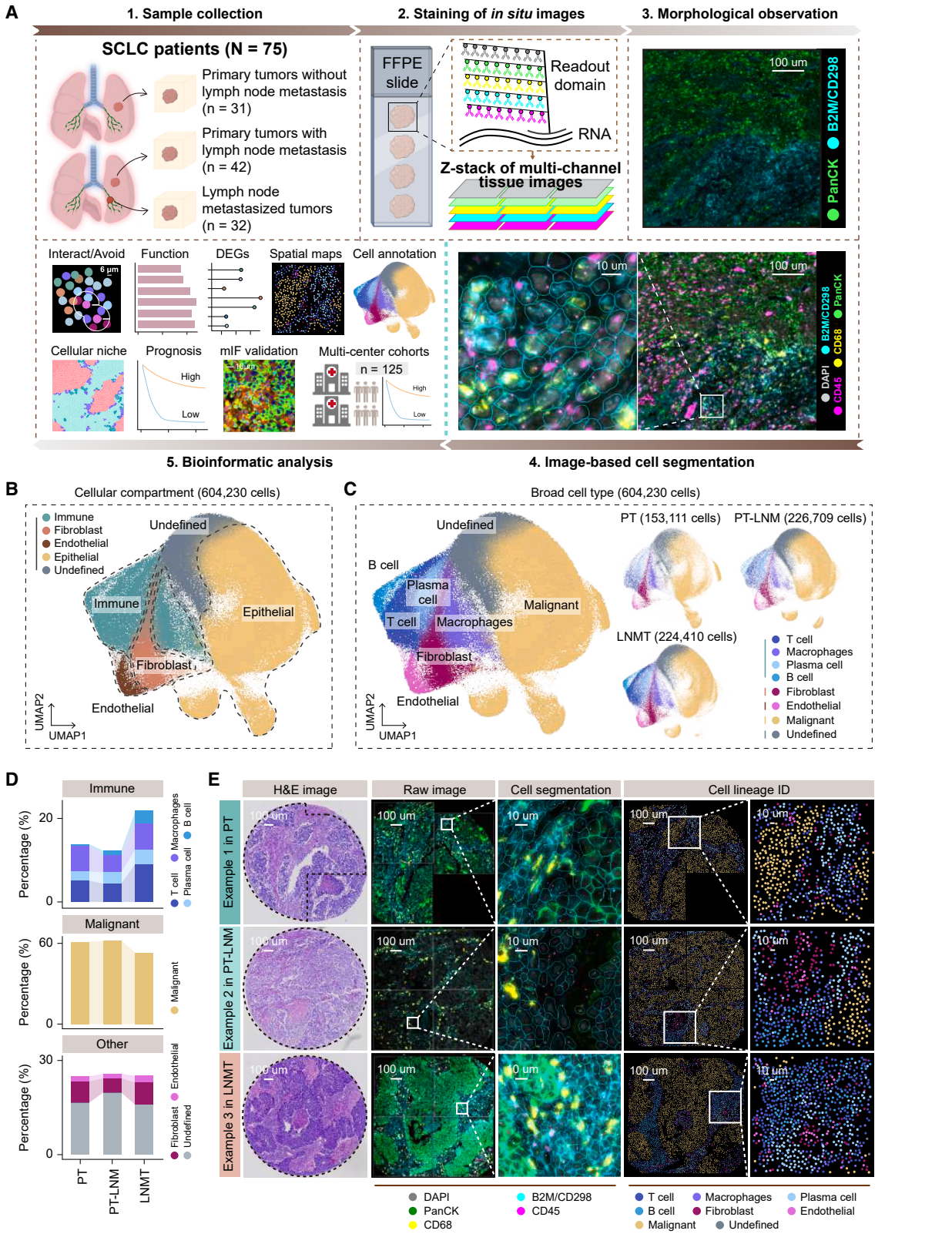

(legend on next page)

TME architecture between primary SCLC tumors and their matched LN metastases (LNMs) is still lacking.

In this study, we aimed to characterize the spatial landscape of SCLC across primary and LN metastatic sites. Using CosMx SMI, we profiled over 600,000 single cells across 105 tumor samples from 75 patients, including primary tumors without LN metastasis (PT), primary tumors with LN metastasis (PT-LNM), and LN metastasized tumors (LNMT). Our goal was to map the cellular diversity, spatial architecture, and tumor microenvironmental changes associated with LNM in SCLC, providing a valuable resource for further investigation into the spatial biology of SCLC progression.

RESULTS

Single-cell spatial transcriptomic atlas of SCLC primary tumors and lymph node metastases

To delineate the TME landscape of SCLC progression, we performed high-plex CosMx SMI with the 1,000-gene panel on 105 primary and metastatic LN samples (31 PTs, 42 PT-LNMs, and 32 LNMTs) from 75 patients (Figures 1A and S1A). Baseline clinical and pathologic variables of the SCLC cohort were displayed in Table S1. Using the specific pretrained segmentation pipeline of CosMx SMI data and rigorous quality control,[23] we profiled approximately 600,000 high-quality single cells and assigned 294 million transcripts across 384 fields of view (FOVs), each covering an area of 510 μm × 510 μm (Figures 1A and S1B–S1D; Table S2). Following batch correction (Figures S1E and S1F), unsupervised clustering identified four major cell compartments based on canonical markers, including epithelial (*n* = 353,268, *EPCAM*), endothelial (*n* = 10,560, *VWF* and *CD34*), fibroblast (*n* = 36,669, *COL1A2* and *ACTA2*), and immune cells (*n* = 97,926, *PTPRC*, *CD68*, *JCHAIN*, and *CD2*) (Figures 1B and S2A), as well as seven broad cell types, including B cells (*n* = 9,678, *CD19* and *MS4A1*), T cells (*n* = 38,149, *CD2*, *CD3D*, and *CD3E*), plasma cells (*n* = 17,100, *JCHAIN*), macrophages (*n* = 32,999, *CD68*), endothelial cells (*n* = 10,560, *PECAM1*, *CD34*, and *VWF*), fibroblasts (*n* = 36,669, *ACTA2*, *COL1A1*, and *COL1A2*), and malignant cells (*n* = 353,268, *EPCAM*, *SFN*, *KRT8*, *KRT18*, *KRT19*, and *CDH1*) (Figures 1C and S2B). Comparative analysis of the cellular composition revealed changes among the conditions, with LNMT showing a significant enrichment of immune cells compared to primary tumors (PT, PT-LNM) (Figures 1D, S2C, and S2D). Spatial mapping uncovered distinct organizational patterns. For example, in metastatic samples (PT-LNM and LNMT), fibroblasts were surrounded by immune cells, a spatial relationship that was not observed in PT samples (Figure 1E). This architecture was validated by matched H&E and immunofluorescence staining, confirming the robustness of our spatial transcriptomic data (Figure 1E). Collectively, these data establish a high-resolution spatial atlas and reveal the heterogeneity and complexity of the TME during LNM in SCLC.

Identification and characterization of metastasis-associated malignant cell subpopulations

We performed uniform manifold approximation and projection (UMAP) analysis to re-cluster 353,268 malignant cells into 13 transcriptionally distinct subclusters (Figure 2A). Tissue distribution analysis revealed that subclusters C5, C6, and C9 were specifically enriched in tumors from patients with LNM (PT-LNM and LNMT) and were largely absent from metastasis-naive PT (Figures 2B and S3A). To explore transcriptional changes of malignant cells associated with LNM, we performed differential gene expression analysis across the malignant cell subclusters to identify key marker genes for these metastasis-associated subclusters (Figure 2C). The results revealed that five genes were significantly up-regulated in C5, 28 genes in C6, and seven genes in C9. Notably, C5, C6, and C9 upregulated genes with established roles in metastasis and cell cycle regulation (e.g., *FYN*, *NR2F2*, *FOS*, *TGFB3*, and *HIF1A*) (Figures 2C and S3B). Additionally, potential gene signatures, including *DHRS2*, *SERPINA1*, and *COL6A2*, were specifically identified for C6 and C9 (Figure S3B). Gene Ontology analysis indicated enrichment for processes involved in cell migration, proliferation, and invasion (Figure 2C). Specifically, the C6 subcluster exhibited a dual signature implicating metabolic reprogramming and immunosuppression, supported by its significant negative correlation with infiltrating immune cells (Figure S3C). Multiplex immunofluorescence (mIF) staining confirmed the presence of FYN+NR2F2+ C5, SERPINA1+DHRS2+ C6, and HIF1A+ COL6A2+ C9 in PT-LNM and LNMT tumors (Figures 2D and S3D). Further examination of the malignant subclusters C5, C6, and C9 across SCLC molecular subtypes revealed that C6 was exclusively enriched in the SCLC-Y subtype, whereas C5 was broadly distributed and C9 was associated with SCLC-N/P subtypes (Figure S3E). To assess whether these subclusters are universal or site-specific adaptations, we analyzed their defining gene signatures in independent, multi-organ metastasis single-cell RNA sequencing (RNA-seq) data from Savchuk et al. cohort.[24] We found that the markers associated with C5, C6, and C9 showed low expression in tumor cells from brain, liver, kidney, or pleural metastases (Figures S4A and S4B), indicating that these subclusters may be LN-specific adaptive programs rather than universal in other metastatic contexts.

Immune cell dynamics and functional reprogramming in lymph node metastasis

We characterized the immune cell composition across PT, PT-LNM, and LNMT and found that B cells and T cells were

Figure 1. Single-cell spatial transcriptomic profiling of the SCLC tumor microenvironment

(A) Schematic workflow. Tissue microarrays containing 105 samples from 75 SCLC patients were analyzed using CosMx SMI (1,000-plex panel), followed by cell segmentation and lineage assignment. Scale bars: 100 μm and 10 μm. Created with BioRender.com.

(B and C) UMAP visualization of 604,230 high-quality cells, colored by (B) major cell compartment and (C) broad cell type (left) or sample group (right).

(D) Stacked bar plots quantifying the relative frequency of broad cell types across PT, PT-LNM, and LNMT.

(E) Representative images validating spatial architecture. For each group (PT, PT-LNM, LNMT): H&E staining, composite CosMx SMI image (DAPI, PanCK, CD68, CD45, B2M/CD298), and spatial map of annotated cell lineages. Scale bars: 100 μm (left) and 10 μm (right).

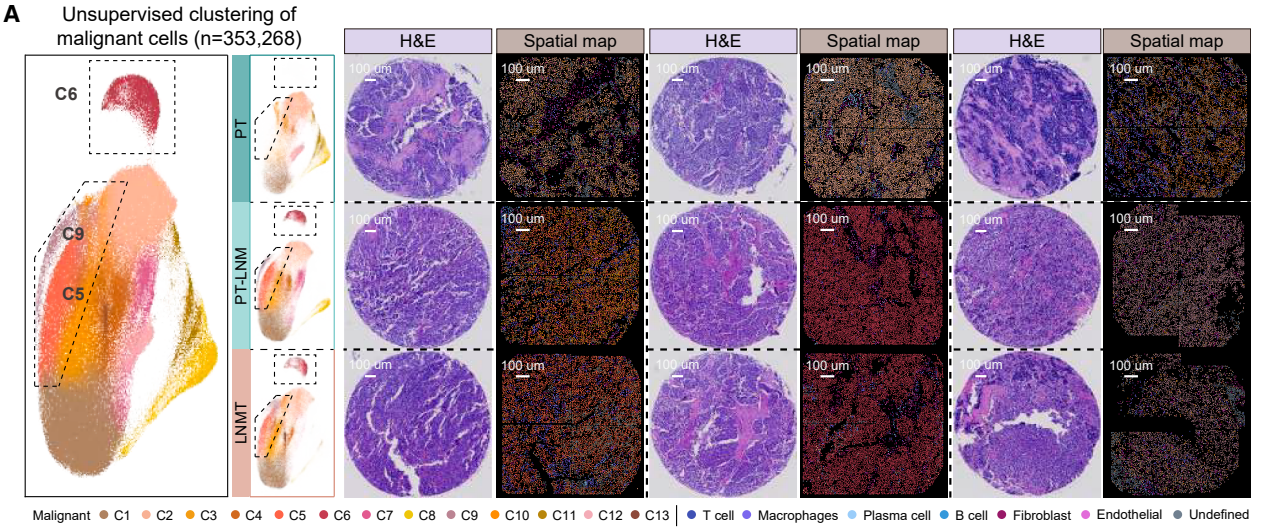

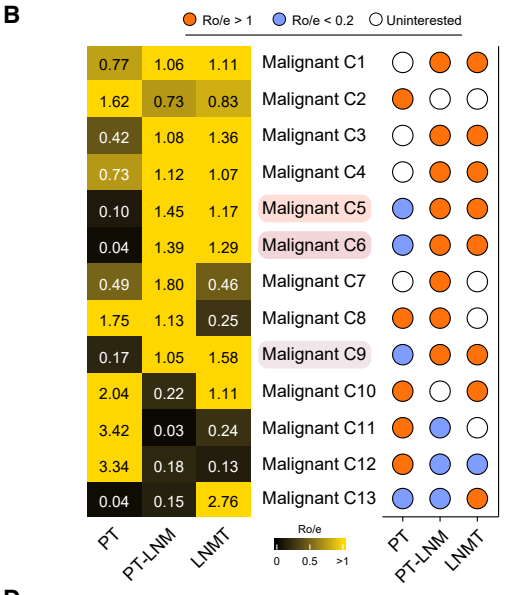

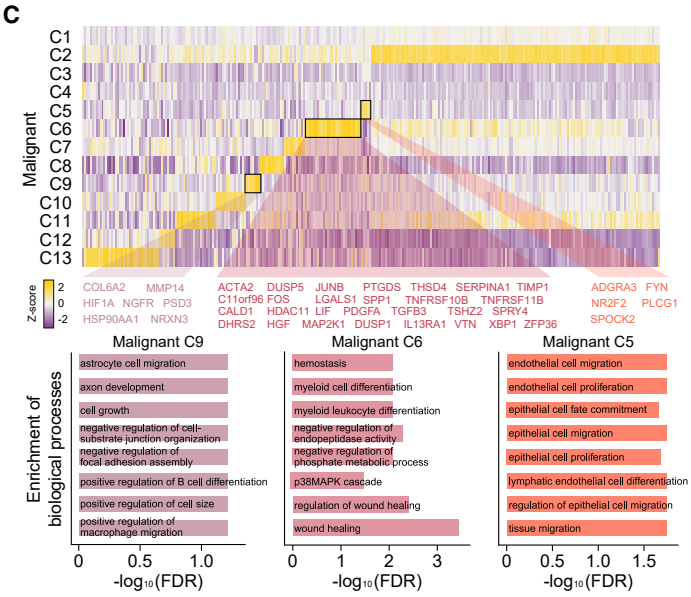

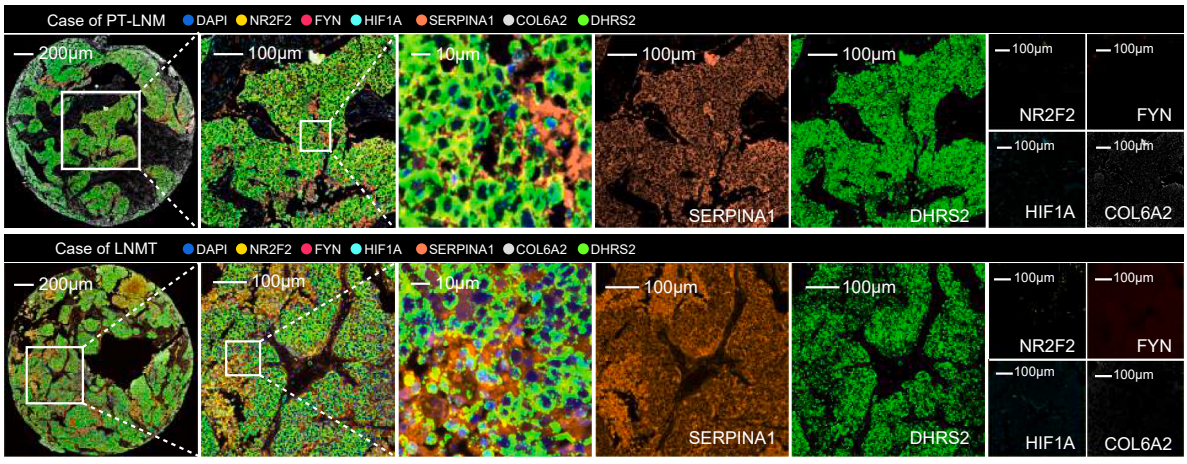

(legend on next page)

significantly more abundant in LNMT than in PT (Figures 1C and S2D). We annotated 38,149 T cells into six subsets, including effector $CD4^+$ T cells, effector $CD8^+$ T cells, inflammatory Tregs, double-negative T cells ([DNTs] $CD3^+CD4^-CD8^-$), exhausted Tregs, and exhausted $CD8^+$ T cells (Figures 3A and S5A). Similarly, 9,678 B cells were classified into four subsets: memory B cells, proliferative B cells, naive B cells, and transitional B cells (Figure 3B and S5B). Comparative analysis revealed a distinct immunosuppressive shift. PTs were enriched for effector $CD4^+$ and $CD8^+$ T cells, whereas PT-LNMs and LNMTs exhibited higher proportions of exhausted and inflammatory Tregs (Figures 3C and 3D). Among B cells, naive B cells were predominant in LNMT, while transitional and proliferative B cells were significantly increased in metastatic samples, suggesting active B cell recruitment and differentiation during LNM (Figure 3D).

To explore molecular heterogeneity beyond cell proportions, we identified differentially expressed genes (DEGs) in each immune cell type for pairwise comparisons (Figure 3E). Interestingly, the magnitude of expression changes between LNMT and PT was strongly correlated with changes between PT-LNM and PT (Spearman's $\rho = 0.73$, $p < 2.2 \times 10^{-16}$), and with changes between LNMT and PT-LNM ($\rho = 0.79$, $p < 2.2 \times 10^{-16}$) (Figure 3F), which implies a continuous transcriptional continuum underlying the LNM process. Monotonic trend analysis further identified a core set of 11 consistently up-regulated and 42 down-regulated genes from PT to PT-LNM to LNMT (Figures 3G and S6). Pathway enrichment analysis of the monotonically up-regulated genes revealed the activation of pathways involved in immune cell recruitment, such as chemokine signaling, cytokine-cytokine receptor interaction, and nuclear factor (NF)-κB signaling, in PT-LNM and LNMT (Figure 3G). These findings collectively underscore the immunosuppressive reprogramming of the TME during LNM in SCLC, linking cellular distribution changes to a coordinated metastasis-associated transcriptional program.

Spatial interaction and avoidance behaviors reveal vascular-immune niche dynamics in SCLC metastasis

To investigate the spatial cell-cell co-localization, we performed interaction/avoidance analyses across PT, PT-LNM, and LNMT (Figure 4A). Despite sharing similar tissue niches, we observed that malignant cells in PT exhibited more interactions with non-cancer cell types (10 pairwise interactions) compared to PT-LNM (five pairwise interactions) (Figures 4B and S7). Notably, the three LNM-associated subclusters (C5, C6, and C9) exhibited spatial immune exclusion-like behavior, characterized by spatial avoidance of the surrounding immune cell populations (Figure 4B). Interestingly, the overall abundance of these subclusters positively correlated with immune cell infiltration (Figures 4B, 4C, and S8A), indicating that their local immune exclusion is a spatially regulated phenomenon, independent of bulk abundance.

The endothelial cells exhibited strong avoidance behaviors with all malignant subpopulations, indicating a vascular-immune niche characterized by indirect tumor-vasculature contact (Figure 4B). In contrast, endothelial cells showed frequent interactions and positive correlations with multiple immune cell types, including macrophages, effector $CD4^+$ T cells, effector $CD8^+$ T cells, memory B cells, and plasma cells (Figures 4B, 4C, and S8B). These interactions were further validated using CellChat analysis, which revealed robust cell-cell signaling links (Figure S9). Notably, perivascular immune cells exhibited distinct functional marker expressions compared to those avoiding endothelial cells across PT, PT-LNM, and LNMT (Figures 4D and S10). In PT, perivascular effector $CD4^+$ T cells expressed higher levels of the immune checkpoint molecule *CTLA-4* compared to non-perivascular cells. In contrast, in PT-LNM and LNMT, perivascular effector $CD4^+$ T cells expressed elevated levels of the cytotoxic markers *GZMA* and *GZMB* (Figures 4D and S10). These findings highlight the functional diversity of immune cells within the vascular niche, which is dynamically reprogrammed during LNM.

Spatial cellular neighborhoods reveal metastasis-associated niches and prognostic immune hotspots

Using SMI imaging and spatial maps, we characterized multicellular communication structures by performing cellular neighborhood (CN) analysis based on the local cellular composition of the 10 nearest neighbors for each cell (Figure 5A). We identified 11, 13, and 15 distinct CNs in PT, PT-LNM, and LNMT, respectively. These CNs were then consolidated into six major spatial structures: tumor compartment, exhausted niche, pan-immune hotspot-1 (PIHs-1), pan-immune hotspot-2 (PIHs-2), B cell-enriched niche, and vascular niche (Figures 5B, S11A, and S11B). Among these, CNs specifically enriched for the LNM-associated malignant subclusters C5, C6, and C9 were predominantly found in PT-LNM and LNMT, with distinct spatial interactions (Figure 5B). In LNMT, C5-enriched CNs were associated with exhausted $CD8^+$ T cells, while C6-enriched CNs were linked to DNTs, specific B cell subsets (Figure 5B). The distribution of CNs varied significantly across PT, PT-LNM, and LNMT. PIHs-2 was exclusive to PT, while B cell-enriched CNs were specific to LNMT. Notably, the abundance of the PIHs-1 was highest in PT (median 1.458%) compared to PT-LNM (0.294%) and LNMT (0.0197%), whereas PT-LNM was enriched in the exhausted tumor niche (median 6.510%) (Figure 5C). However,

Figure 2. Malignant cell heterogeneity associated with lymph node metastasis

(A) UMAP plots of 353,268 malignant cells colored by subcluster, with matched H&E and spatial maps from representative PT, PT-LNM, and LNMT samples. Scale bars, 100 μm.

(B) Tissue distribution of subclusters. Heatmap showing the Ro/r scores of each malignant subcluster across PT, PT-LNM, and LNMT groups (left). Orange dots represent enriched states (Ro/e > 1) and blue dots represent depleted states (Ro/e < 0.2) (right).

(C) Heatmap of differentially expressed genes for key malignant cell subclusters. Bar plots showing the top enriched pathways in C5, C6, and C9 subclusters.

(D) Representative mIF images confirming the co-expression of SERPINA1 and DHRS2 (C6 markers) in PT-LNM and LNMT samples. Scale bars: 200 μm, 100 μm, and 10 μm.

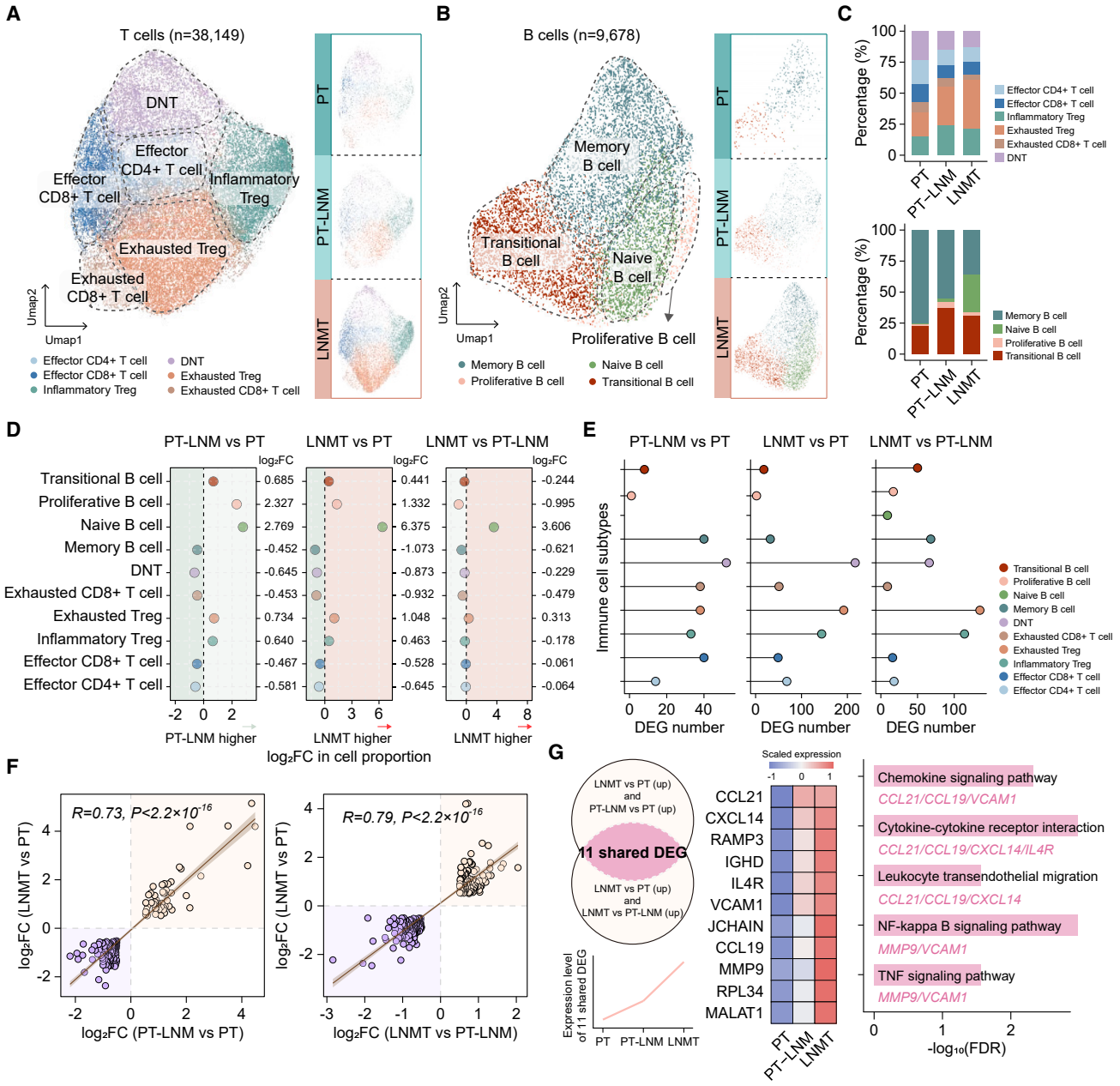

Figure 3. Heterogeneity of T and B cell landscapes in SCLC lymph node metastasis

(A and B) UMAP plots visualizing the annotated subsets of (A) T cells (n = 38,149) and (B) B cells (n = 9,678) across PT, PT-LNM, and LNMT samples. Each dot represents a single cell, colored by its respective subtype.

(C) Stacked bar plots showing the relative proportions of T cell (top) and B cell (bottom) subsets across PT, PT-LNM, and LNMT.

(D) Lollipop plot illustrating the $\log_2$ fold change (FC) in the proportion of each T cell and B cell subset for the comparisons PT-LNM vs. PT, LNMT vs. PT, and LNMT vs. PT-LNM.

(E) Lollipop plot showing the number of DEGs identified in each immune cell type for the three comparisons.

(F) Scatterplots demonstrating the correlation between the $\log_2$FC values of DEGs across the indicated pairwise comparisons. Spearman's correlation coefficient (ρ) and p value are shown.

(G) Conserved transcriptional trends and pathway activation. (Left) Venn diagram identifying 11 DEGs with a monotonic increase from PT to PT-LNM to LNMT. (Middle) Heatmap showing the scaled expression of these 11 DEGs across sample types. (Right) Bar plots of the top KEGG pathways enriched for the shared up-regulated DEGs.

CellPress
OPEN ACCESS

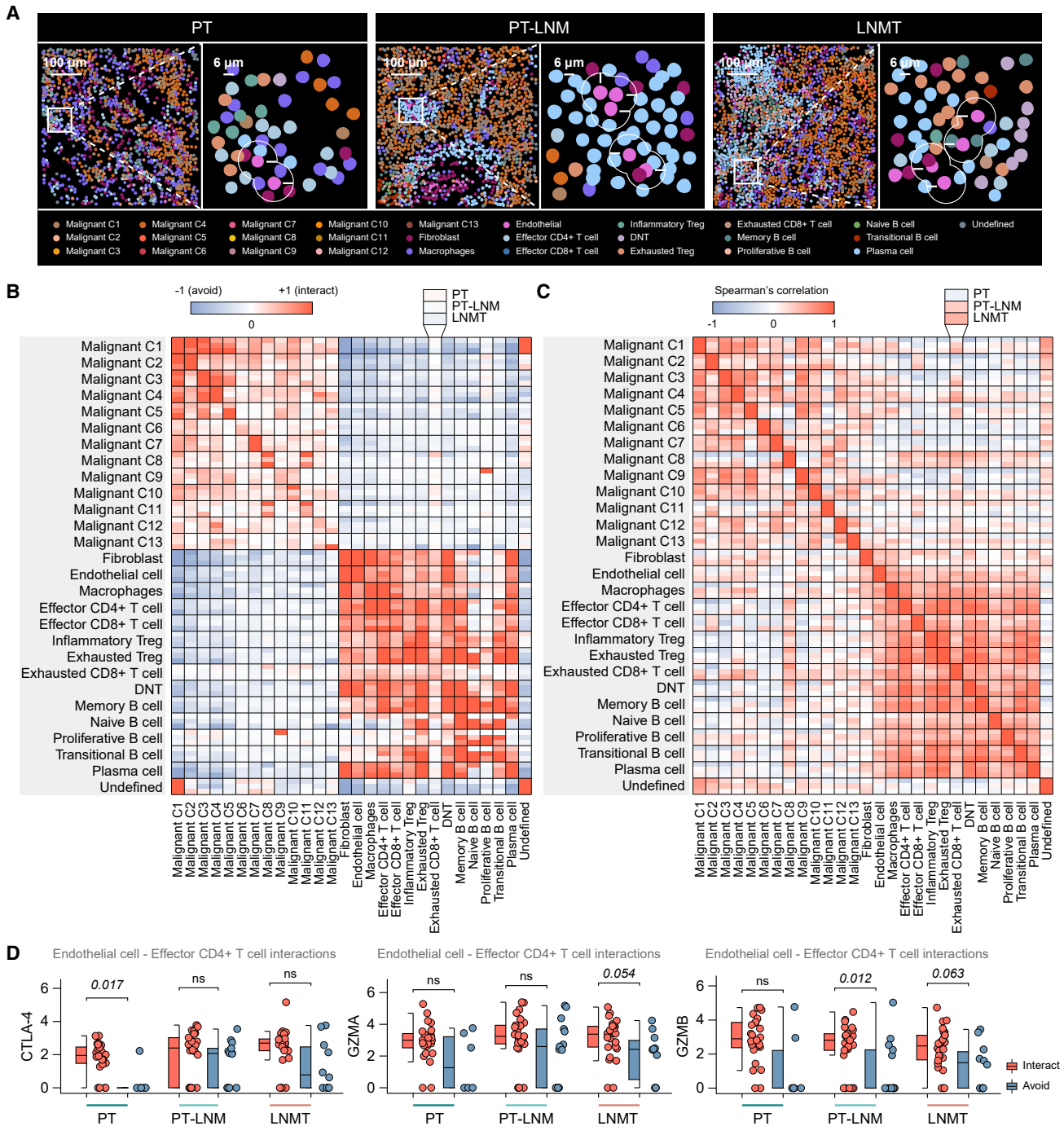

Figure 4. Single-cell spatial analysis unravels cell-cell co-localization profiles

(A) Schematic illustrating the cell-cell co-localization across PT, PT-LNM, and LNMT. Scale bars: 100 μm (overview) and 6 μm (detail, right panels).

(B) Heatmaps summarizing significant pairwise interactions (red) or avoidance (blue) between all cell types in PT (top), PT-LNM (middle), and LNMT (bottom).

(C) Heatmaps of Spearman's correlation coefficients for pairwise cell type abundances. Red indicates positive correlation and blue indicates negative correlation.

(D) Boxplots comparing the expression of *CTLA-4*, *GZMA*, and *GZMB* in effector $CD4^+$ T cells that are spatially interacting with (red) or avoiding (blue) endothelial cells. Data are represented as the median and interquartile range (IQR), and whiskers indicate maximum and minimum values. The *p* values from two-sided Wilcoxon signed-rank tests; ns denotes not significant ($p > 0.05$).

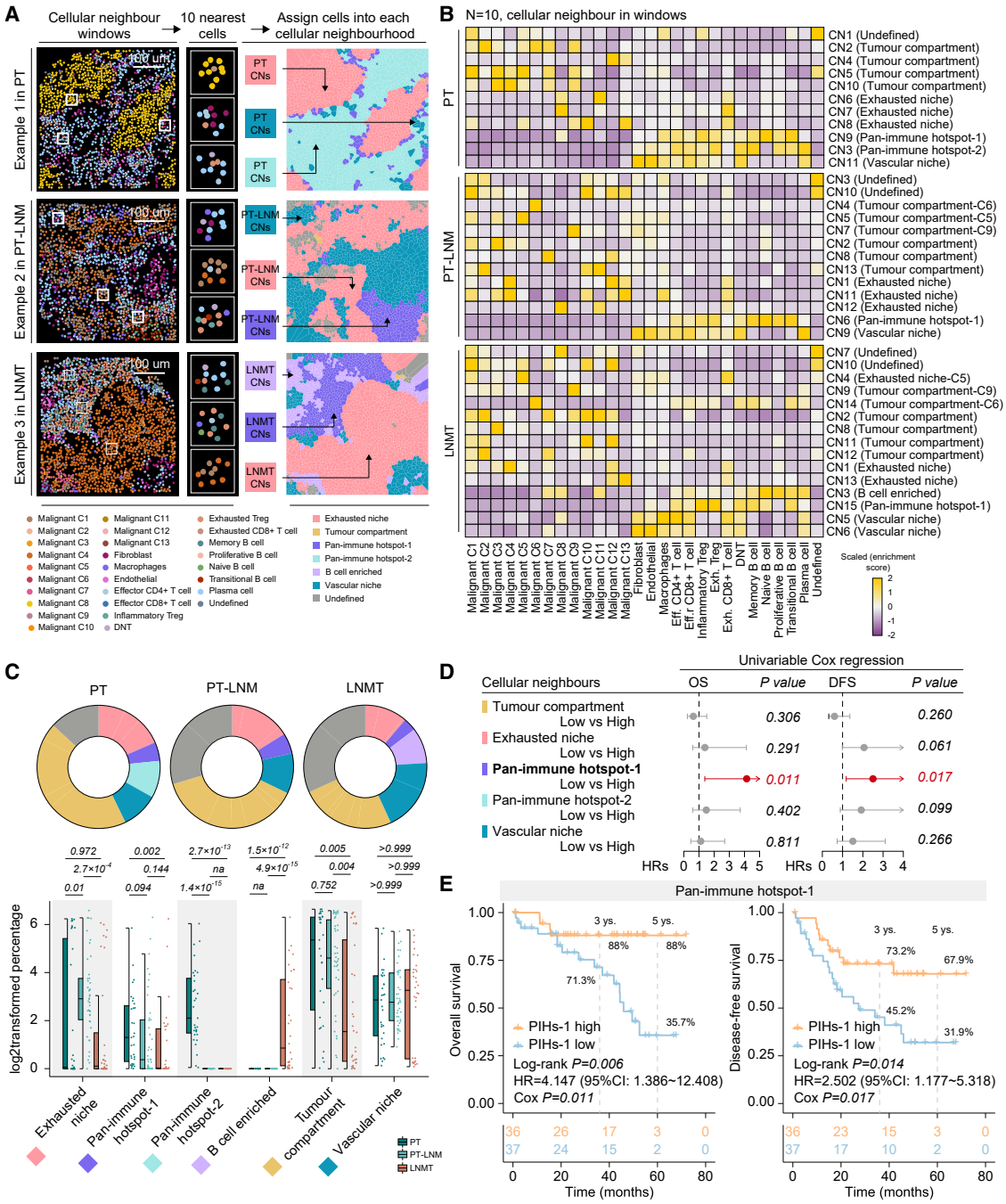

Figure 5. Spatial CNs correlated with LNM and survival

(A) Spatial maps (left) of CN assignment in representative PT, PT-LNM, and LNMT samples. (Right) Corresponding Voronoi diagram representations of the CNs. Scale bars, 100 μm.

(B) Heatmaps showing the cellular composition within each identified CN across PT, PT-LNM, and LNMT, calculated based on the composition of the $N = 10$ nearest neighboring cells. A total of 11, 13, and 15 CNs were identified in PT, PT-LNM, and LNMT, respectively.

(C) Pie plots showing the relative frequency of the six major CNs in PT, PT-LNM, and LNMT. Boxplots comparing the $\log_2$-transformed percentage abundance of specific CNs among PT, PT-LNM, and LNMT. Data are represented as the median and IQR, and whiskers indicate maximum and minimum values. The p values were calculated using two-sided Wilcoxon signed-rank tests.

(D) Forest plots from univariable Cox regression analysis showing the HR and 95% confidence interval for each CN's association with OS and DFS.

(E) Survival analysis based on PIHs-1 abundance. Kaplan-Meier curves for OS (left) and DFS (right) of 73 SCLC patients stratified into high (>median) and low (≤median) PIHs-1 abundance groups. p values were calculated using the log rank test.

no significant differences were observed in the vascular niche (Figure 5C). We further validated the presence of major immune cell types in pan-immune hotspots of PT and PT-LNM using mIF images (Figure S11C). These results suggest that the reorganization of spatial immune and tumor niches is a critical feature of metastatic progression.

To evaluate the clinical relevance of spatial organization, we stratified patients based on CN abundance. Univariable and survival analysis revealed that high abundance of the PIHs-1 was significantly associated with superior overall survival and disease-free survival (DFS) (Figures 5D and 5E). However, the abundance of individual immune cell types was not predictive, highlighting that prognostic value lies in spatial architecture, not merely cellular composition (Figure S12A). Multivariable Cox regression analysis confirmed that PIHs-1 is an independent prognostic factor for overall survival (OS) (hazard ratio [HR] = 4.418, 95% confidence interval [CI]: 1.415–13.795, $p = 0.011$) and showed a strong association with DFS (HR = 2.195, 95% CI: 0.993–4.852, $p = 0.052$), after adjusting for clinicopathological variables (Table S3; Figure S12B). Furthermore, the percentage of PIHs-1 did not show significant differences across SCLC-A, SCLC-N, SCLC-P, and SCLC-Y subtypes (Figure S12C), indicating the presence of a universal immune microenvironment that is independent of SCLC molecular subtype. To translate this spatial discovery into a clinically applicable biomarker, we derived a 20-gene signature from its defining transcripts and validated it in two independent, multicenter bulk RNA-seq cohorts of SCLC. Patients were stratified into PIHs-1 high and PIHs-1 low subgroups based on the median PIHs-1 signature score. Patients with a low PIHs-1 signature score had significantly poor OS (log rank $p = 0.018$; HR = 1.756, 95% CI: 1.095–2.816, $p = 0.019$), confirming the robust and generalizable prognostic value of this spatial immune microenvironment feature beyond our discovery cohort (Figure S12D).

DISCUSSION

Spatial molecular imaging technologies now enable spatial multi-omics profiling of archival formalin-fixed and paraffin-embedded tissues at the cellular and subcellular resolution, preserving the native tissue architecture essential for studying cellular ecosystems and their prognostic implications. Here, we leveraged high-plex, spatial single-cell transcriptomics to reveal the TME landscape of SCLC LNM using CosMx SMI. By analyzing a large, clinically annotated cohort of matched primary and metastatic lesions, we provide a comprehensive spatial atlas that moves beyond cataloging cellular diversity to reveal the spatial organization and niche-specific adaptation underlying metastatic progression.

While previous studies on SCLC metastasis have provided foundational insights through cell line models, bulk analyses, or single-cell sequencing of dissociated cells,[25–28] these approaches inherently lack the spatial context critical for understanding the functional architecture of metastatic sites. Recent pioneering spatial studies have begun mapping SCLC architecture, revealing features such as immune cell colonies and neuroendocrine state organization.[15,29,30] However, a systematic, high-resolution comparative spatial analysis of the TME architecture between primary tumors and their matched LNMs has been lacking. Our study directly addresses this critical gap. We identified several metastasis-associated malignant subpopulations enriched in LNM samples. These subpopulations express markers associated with metastasis and adaptation, such as FYN, NR2F2, and HIF1A,[31,32] and exhibit transcriptional programs involving metabolic reprogramming, angiogenesis, and extracellular matrix remodeling. Crucially, by integrating our spatial signatures with an independent multi-organ metastasis single-cell atlas,[24] the defining transcriptional programs of C5, C6, and C9 are predominantly specific to LNM and are negligible in the brain, liver, or other visceral sites. However, as previously described in previous studies,[33,34] LNs are immunologically specialized organs that host dynamic tumor-immune interactions that are distinct from those in visceral sites. Therefore, the observed transcriptional differences may reflect context-specific immune adaptations rather than intrinsic metastasis-driving programs. The immune microenvironment of the LN, with its unique immune and stromal components, may significantly influence the tumor's transcriptional landscape. The functional implications of these adaptive states are underscored by their spatial behavior. Notably, subclusters C5, C6, and C9 exhibited significant spatial avoidance of immune cells, an "immune-exclusion" phenotype occurring despite a positive correlation with overall immune cell abundance in the tissue. This suggests an active, localized mechanism of immune evasion within the LN niche. Therapeutically, these subclusters present potential targets for modulating metastatic immune microenvironments. For example, targeting *FYN* could improve the effectiveness of immune checkpoint blockade (ICB) in preclinical models by decreasing tumor cell migration and increasing T cell infiltration,[35,36] while *NR2F2* inhibition could make tumors more susceptible to ICB.[37,38]

The transition from primary tumors to metastatic LNs is characterized by a progressive shift toward an immunosuppressive TME, characterized by Tregs, B cell polarization, and vascular niche reprogramming. The dominance of exhausted Tregs and the decrease of effector $CD8^+$ T cells in metastatic tumors are consistent with chronic antigen exposure and sustained activation of immune checkpoint pathways such as *PD-1* and *CTLA-4*.[39] While previous single-cell and proteo-transcriptomic studies had highlighted the roles of immune cell infiltration, stromal reprogramming, and neuroendocrine states in SCLCs,[3,17,18,40] spatial interaction analysis revealed dynamic vascular-immune niche rewiring. While endothelial cells spatially avoided malignant subclusters, they engaged in frequent interactions with immune cells, suggesting that the tumor vasculature plays an important role in immune modulation during LNM. These findings are consistent with a recent study that highlighted the role of the vasculature in modulating the immune response within tumors.[41] Notably, perivascular effector $CD4^+$ T cells in metastatic sites expressed elevated cytotoxic markers (*GZMA*/*GZMB*), which contrasts with the CTLA-4+ T cell populations in primary tumors. These results suggest that the perivascular space in metastases may be co-opted to sustain a cytolytic, yet potentially dysfunctional immune response, which is

supported by the enrichment of NF-κB and tumor necrosis factor signaling pathways in metastatic samples.[42]

Our study also provided valuable prognostic insights by identifying PIHs-1, a spatial immune niche enriched in specific tumor and immune cell populations. This PIHs-1, a multicellular niche of coordinated T/B cell positioning, is an independent favorable prognostic factor. Its prognostic value was independent of the abundance of any single immune cell type and consistent across SCLC molecular subtypes. These findings demonstrated that spatial architecture, not just cellular composition, dictates clinical outcome, aligning with growing evidence of the importance of spatial immune structures over mere immune cell abundance in determining patient outcomes and therapeutic response.[43–47] This PIHs-1 architecture may represent a "spatial checkpoint" where specific cellular positioning enables productive anti-tumor immunity. Furthermore, the successful derivation and validation of a PIHs-1-derived gene signature in independent bulk RNA-seq cohorts underscores its potential as a non-spatial, transcriptomic biomarker for patient stratification. This bridges our high-resolution spatial discovery with practical clinical application. Future prospective studies are warranted to standardize this signature and evaluate its utility in guiding therapy.

In conclusion, our high-resolution, single-cell spatial atlas delineates the cellular and spatial heterogeneity of the SCLC TME during LNM. We uncover distinct, LN-specific malignant cell states, reveal dynamic vascular-immune crosstalk that is reprogrammed during metastasis, and define a prognostic spatial immune architecture whose organization is more informative than mere cellular abundance. Collectively, these findings advance our understanding of SCLC LN metastasis biology beyond bulk or single-cell dissociation studies and establish a valuable foundational resource for future mechanistic exploration and the development of spatially informed biomarkers and therapeutic strategies in SCLC.

Limitations of the study

Several limitations of our study should be noted. First, our spatial analysis focused exclusively on LN metastases; the LN-specific TME we describe may not generalize to all metastatic niches and their spatial architecture in visceral organs remains to be mapped. Second, the 1,000-plex CosMx SMI panel, while providing high sensitivity and quantitative spatial profiling at single-cell resolution, has relatively limited gene coverage and inherently limits unbiased discovery of novel biological programs and precludes high-resolution delineation of certain cellular or biological states dependent on excluded markers. Future studies leveraging spatial technologies with more gene coverage (e.g., CosMx 6K or Xenium 5K) will be essential to build upon this foundational spatial map and fully resolve the spectrum of cellular plasticity in the TME. Third, while we used the field-standard "Cellpose" algorithm and rigorous post-segmentation QC, potential inaccuracies in single-cell segmentation inherent to all highly multiplexed imaging technologies could influence fine-grained spatial metrics such as CN definitions. Future improvements in segmentation algorithms may further refine such analyses. Finally, although we identified key metastatic-associated cell populations and prognosis-related spatial immune hotspot, further validation in larger cohorts or through clinical trials will be necessary to establish its robustness and utility as a clinical biomarker. Translating these spatially defined niches and cell states into therapeutic strategies will require functional interrogation in preclinical models.

RESOURCE AVAILABILITY

Lead contact

Further information and requests for resources should be directed to and will be fulfilled by the lead contact, Lin Yang (yanglin@cicams.ac.cn).

Materials availability

This study did not generate new unique reagents.

Data and code availability

- The raw CosMx SMI data in this study have been deposited in Zenodo database (https://doi.org/10.5281/zenodo.15104582). All data analysis was performed using publicly available software, packages, and tools, as described in the STAR Methods section.
- The code from this manuscript is available at https://github.com/ZhoulabCPH/SCLC-LNM-SMI.git.
- Any additional information required to reanalyze the data reported in this work is available from the lead contact upon request.

ACKNOWLEDGMENTS

This study was supported by the Beijing Municipal Science & Technology Commission (Z221100007422011), the CAMS Innovation Fund for Medical Sciences (CIFMS) (2023-I2M-2-004 and 2024-I2M-C&T-A-005), and the National High Level Hospital Clinical Research Funding (LC2024L01).

AUTHOR CONTRIBUTIONS

Conceptualization, M. Zhou and L.Y.; methodology, Z.Z., D.W., and J.W.; formal analysis, Z.Z. and M. Zhai; resources: L.Y., R.C., F.Y., L.L., and L.G.; writing – original draft, Z.Z. and D.W.; writing – review and editing, Z.Z., L.Y., and M. Zhou; project administration, L.Y. and M. Zhou; supervision, J.Y., L.Y., and M. Zhou; funding, J.Y. and L.Y. All the authors read and approved the final manuscript.

DECLARATION OF INTERESTS

J.W. is an employee at JMDNA Bio-Medical Technology.

STAR★METHODS

Detailed methods are provided in the online version of this paper and include the following:

- KEY RESOURCES TABLE
- EXPERIMENTAL MODEL AND STUDY PARTICIPANT DETAILS
- METHOD DETAILS
  - CosMx SMI data acquisition and processing
  - Multiplex immunofluorescence (mIF)
  - Immunohistochemistry (IHC)
- QUANTIFICATION AND STATISTICAL ANALYSIS
  - Dimensionality reduction and clustering
  - Cell type annotation
  - Tissue distribution preference
  - Differential expression and functional analysis
  - Cell-cell interaction/avoidance analysis
  - Cellular neighborhood (CN) identification
  - Public single-cell RNA-seq data processing
  - Public bulk RNA-seq data processing

- Survival analysis
- Statistical analysis

SUPPLEMENTAL INFORMATION

Supplemental information can be found online at https://doi.org/10.1016/j.xcrm.2026.102713.

Received: September 19, 2025
Revised: January 20, 2026
Accepted: February 27, 2026
Published: March 30, 2026

REFERENCES

1. Gazdar, A.F., Bunn, P.A., and Minna, J.D. (2017). Small-cell lung cancer: what we know, what we need to know and the path forward. Nat. Rev. Cancer *17*, 725–737. https://doi.org/10.1038/nrc.2017.87.
2. Kim, S.Y., Park, H.S., and Chiang, A.C. (2025). Small Cell Lung Cancer: A Review. JAMA *333*, 1906–1917. https://doi.org/10.1001/jama.2025.0560.
3. Tian, Y., Li, Q., Yang, Z., Zhang, S., Xu, J., Wang, Z., Bai, H., Duan, J., Zheng, B., Li, W., et al. (2022). Single-cell transcriptomic profiling reveals the tumor heterogeneity of small-cell lung cancer. Signal Transduct. Target. Ther. *7*, 346. https://doi.org/10.1038/s41392-022-01150-4.
4. Simpson, K.L., Rothwell, D.G., Blackhall, F., and Dive, C. (2025). Challenges of small cell lung cancer heterogeneity and phenotypic plasticity. Nat. Rev. Cancer *25*, 447–462. https://doi.org/10.1038/s41568-025-00803-0.
5. George, J., Maas, L., Abedpour, N., Cartolano, M., Kaiser, L., Fischer, R.N., Scheel, A.H., Weber, J.P., Hellmich, M., Bosco, G., et al. (2024). Evolutionary trajectories of small cell lung cancer under therapy. Nature *627*, 880–889. https://doi.org/10.1038/s41586-024-07177-7.
6. Gardner, E.E., Earlie, E.M., Li, K., Thomas, J., Hubisz, M.J., Stein, B.D., Zhang, C., Cantley, L.C., Laughney, A.M., and Varmus, H. (2024). Lineage-specific intolerance to oncogenic drivers restricts histological transformation. Science (New York, N.Y.) *383*, eadj1415. https://doi.org/10.1126/science.adj1415.
7. De Jonghe, J., Opzoomer, J.W., Vilas-Zornoza, A., Nilges, B.S., Crane, P., Vicari, M., Lee, H., Lara-Astiaso, D., Gross, T., Morf, J., et al. (2024). scTrends: A living review of commercial single-cell and spatial omic technologies. Cell Genom. *4*, 100723. https://doi.org/10.1016/j.xgen.2024.100723.
8. Gulati, G.S., D'Silva, J.P., Liu, Y., Wang, L., and Newman, A.M. (2025). Profiling cell identity and tissue architecture with single-cell and spatial transcriptomics. Nat. Rev. Mol. Cell Biol. *26*, 11–31. https://doi.org/10.1038/s41580-024-00768-2.
9. Lim, H.J., Wang, Y., Buzdin, A., and Li, X. (2025). A practical guide for choosing an optimal spatial transcriptomics technology from seven major commercially available options. BMC Genom. *26*, 47. https://doi.org/10.1186/s12864-025-11235-3.
10. Chang, J., Lu, J., Liu, Q., Xiang, T., Zhang, S., Yi, Y., Li, D., Liu, T., Liu, Z., Chen, X., et al. (2025). Single-cell multi-stage spatial evolutional map of esophageal carcinogenesis. Cancer Cell *43*, 380–397.e7. https://doi.org/10.1016/j.ccell.2025.02.009.
11. Love, N.R., Williams, C., Killingbeck, E.E., Merleev, A., Saffari Doost, M., Yu, L., McPherson, J.D., Mori, H., Borowsky, A.D., Maverakis, E., and Kiuru, M. (2024). Melanoma progression and prognostic models drawn from single-cell, spatial maps of benign and malignant tumors. Sci. Adv. *10*, eadm8206. https://doi.org/10.1126/sciadv.adm8206.
12. Zhang, Q., Abdo, R., Iosef, C., Kaneko, T., Cecchini, M., Han, V.K., and Li, S.S.C. (2022). The spatial transcriptomic landscape of non-small cell lung cancer brain metastasis. Nat. Commun. *13*, 5983. https://doi.org/10.1038/s41467-022-33365-y.
13. Yeh, C.Y., Aguirre, K., Laveroni, O., Kim, S., Wang, A., Liang, B., Zhang, X., Han, L.M., Valbuena, R., Bassik, M.C., et al. (2024). Mapping spatial organization and genetic cell-state regulators to target immune evasion in ovarian cancer. Nat. Immunol. *25*, 1943–1958. https://doi.org/10.1038/s41590-024-01943-5.
14. Shiau, C., Cao, J., Gong, D., Gregory, M.T., Caldwell, N.J., Yin, X., Cho, J.W., Wang, P.L., Su, J., Wang, S., et al. (2024). Spatially resolved analysis of pancreatic cancer identifies therapy-associated remodeling of the tumor microenvironment. Nat. Genet. *56*, 2466–2478. https://doi.org/10.1038/s41588-024-01890-9.
15. Chen, H., Deng, C., Gao, J., Wang, J., Fu, F., Wang, Y., Wang, Q., Zhang, M., Zhang, S., Fan, F., et al. (2025). Integrative spatial analysis reveals tumor heterogeneity and immune colony niche related to clinical outcomes in small cell lung cancer. Cancer Cell *43*, 519–536.e5. https://doi.org/10.1016/j.ccell.2025.01.012.
16. Zhang, Z., Sun, X., Liu, Y., Zhang, Y., Yang, Z., Dong, J., Wang, N., Ying, J., Zhou, M., and Yang, L. (2024). Spatial Transcriptome-Wide Profiling of Small Cell Lung Cancer Reveals Intra-Tumoral Molecular and Subtype Heterogeneity. Adv. Sci. *11*, e2402716. https://doi.org/10.1002/advs.202402716.
17. Jin, Y., Wu, Y., Reuben, A., Zhu, L., Gay, C.M., Wu, Q., Zhou, X., Mo, H., Zheng, Q., Ren, J., et al. (2024). Single-cell and spatial proteo-transcriptomic profiling reveals immune infiltration heterogeneity associated with neuroendocrine features in small cell lung cancer. Cell Discov. *10*, 93. https://doi.org/10.1038/s41421-024-00703-x.
18. Desai, P., Takahashi, N., Kumar, R., Nichols, S., Malin, J., Hunt, A., Schultz, C., Cao, Y., Tillo, D., Nousome, D., et al. (2024). Microenvironment shapes small-cell lung cancer neuroendocrine states and presents therapeutic opportunities. Cell Rep. Med. *5*, 101610. https://doi.org/10.1016/j.xcrm.2024.101610.
19. Zhai, M., Zhang, Z., Dong, J., Li, Z., Cao, Y., Chen, R., Zhou, M., and Yang, L. (2025). Spatial proteomic profiling reveals conserved prognostic immune microenvironment features across molecular subtypes in small cell lung cancer. Pharmacol. Res. *222*, 108048. https://doi.org/10.1016/j.phrs.2025.108048.
20. Zhang, Y., Liu, S., Chen, J., Chen, R., Yang, Z., Sheng, R., Li, X., Wang, T., Liu, H., Yang, F., et al. (2025). Deep learning-based histomorphological subtyping and risk stratification of small cell lung cancer from hematoxylin and eosin-stained whole slide images. Genome Med. *17*, 98. https://doi.org/10.1186/s13073-025-01526-5.
21. Zhang, Z., Zhai, M., Bao, S., Sun, X., Chen, R., Wang, B., Yang, F., Yang, L., and Zhou, M. (2026). Integrative multi-omics profiling deciphers tumor microenvironment heterogeneity and immunotherapy vulnerabilities in lung neuroendocrine carcinomas. J. Adv. Res. *81*, 797–808. https://doi.org/10.1016/j.jare.2025.06.017.
22. Zhang, Z., Wu, X., Bao, S., Sun, X., Yang, F., Zhang, Y., Yang, Z., Zhang, L., Chen, R., Xing, P., et al. (2025). Proteogenomic Characterization of High-Grade Lung Neuroendocrine Carcinoma Deciphers Molecular Diversity and Potential Biomarkers of Different Histological Subtypes in Chinese Population. Research *8*, 0671. https://doi.org/10.34133/research.0671.
23. He, S., Bhatt, R., Brown, C., Brown, E.A., Buhr, D.L., Chantranuvatana, K., Danaher, P., Dunaway, D., Garrison, R.G., Geiss, G., et al. (2022). High-plex imaging of RNA and proteins at subcellular resolution in fixed tissue by spatial molecular imaging. Nat. Biotechnol. *40*, 1794–1806. https://doi.org/10.1038/s41587-022-01483-z.
24. Savchuk, S., Gentry, K.M., Wang, W., Carleton, E., Biagi-Junior, C.A.O., Luthria, K., Yalçın, B., Ni, L., Farnsworth, H.C., Davis, R.A., et al. (2025). Neuronal activity-dependent mechanisms of small cell lung cancer pathogenesis. Nature *646*, 1232–1242. https://doi.org/10.1038/s41586-025-09492-z.
25. Yang, D., Qu, F., Cai, H., Chuang, C.H., Lim, J.S., Jahchan, N., Grüner, B.M., S Kuo, C., Kong, C., Oudin, M.J., et al. (2019). Axon-like protrusions

promote small cell lung cancer migration and metastasis. eLife *8*, e50616. https://doi.org/10.7554/eLife.50616.

26. Wu, Z., Su, J., Li, F.L., Chen, T., Mayner, J., Engler, A., Ma, S., Li, Q., and Guan, K.L. (2023). YAP silencing by RB1 mutation is essential for small-cell lung cancer metastasis. Nat. Commun. *14*, 5916. https://doi.org/10.1038/s41467-023-41585-z.
27. Lissa, D., Takahashi, N., Desai, P., Manukyan, I., Schultz, C.W., Rajapakse, V., Velez, M.J., Mulford, D., Roper, N., Nichols, S., et al. (2022). Heterogeneity of neuroendocrine transcriptional states in metastatic small cell lung cancers and patient-derived models. Nat. Commun. *13*, 2023. https://doi.org/10.1038/s41467-022-29517-9.
28. Best, S.A., Hess, J.B., Souza-Fonseca-Guimaraes, F., Cursons, J., Kersbergen, A., Dong, X., Rautela, J., Hyslop, S.R., Ritchie, M.E., Davis, M.J., et al. (2020). Harnessing Natural Killer Immunity in Metastatic SCLC. J. Thorac. Oncol. *15*, 1507–1521. https://doi.org/10.1016/j.jtho.2020.05.008.
29. Jin, Y., Wu, Y., Reuben, A., Zhu, L., Gay, C.M., Wu, Q., Zhou, X., Mo, H., Zheng, Q., Ren, J., et al. (2024). Author Correction: Single-cell and spatial proteo-transcriptomic profiling reveals immune infiltration heterogeneity associated with neuroendocrine features in small cell lung cancer. Cell Discov. *10*, 126. https://doi.org/10.1038/s41421-024-00755-z.
30. Sun, Y., Zhang, M., Zhao, Y., Yan, Y., Wang, L., Liu, X., Xia, S., Wang, B., Zhang, X., and Wang, Y. (2025). Spatial transcriptomics reveals macrophage domestication by epithelial cells promotes immunotherapy resistance in small cell lung cancer. npj Precis. Oncol. *9*, 252. https://doi.org/10.1038/s41698-025-01005-5.
31. Massagué, J., and Obenauf, A.C. (2016). Metastatic colonization by circulating tumour cells. Nature *529*, 298–306. https://doi.org/10.1038/nature17038.
32. Pastushenko, I., Brisebarre, A., Sifrim, A., Fioramonti, M., Revenco, T., Boumahdi, S., Van Keymeulen, A., Brown, D., Moers, V., Lemaire, S., et al. (2018). Identification of the tumour transition states occurring during EMT. Nature *556*, 463–468. https://doi.org/10.1038/s41586-018-0040-3.
33. Ji, H., Hu, C., Yang, X., Liu, Y., Ji, G., Ge, S., Wang, X., and Wang, M. (2023). Lymph node metastasis in cancer progression: molecular mechanisms, clinical significance and therapeutic interventions. Signal Transduct. Target. Ther. *8*, 367. https://doi.org/10.1038/s41392-023-01576-4.
34. Lohinai, Z., Megyesfalvi, Z., Suda, K., Harko, T., Ren, S., Moldvay, J., Laszlo, V., Rivard, C., Dome, B., and Hirsch, F.R. (2019). Comparative expression analysis in small cell lung carcinoma reveals neuroendocrine pattern change in primary tumor versus lymph node metastases. Transl. Lung Cancer Res. *8*, 938–950. https://doi.org/10.21037/tlcr.2019.11.30.
35. Debackere, K., Marcelis, L., Demeyer, S., Vanden Bempt, M., Mentens, N., Gielen, O., Jacobs, K., Broux, M., Verhoef, G., Michaux, L., et al. (2021). Fusion transcripts FYN-TRAF3IP2 and KHDRBS1-LCK hijack T cell receptor signaling in peripheral T-cell lymphoma, not otherwise specified. Nat. Commun. *12*, 3705. https://doi.org/10.1038/s41467-021-24037-4.
36. Peng, W., Liu, C., Xu, C., Lou, Y., Chen, J., Yang, Y., Yagita, H., Overwijk, W.W., Lizée, G., Radvanyi, L., and Hwu, P. (2012). PD-1 blockade enhances T-cell migration to tumors by elevating IFN-gamma inducible chemokines. Cancer Res. *72*, 5209–5218. https://doi.org/10.1158/0008-5472.CAN-12-1187.
37. Tian, Y., Zhai, X., Han, A., Zhu, H., and Yu, J. (2019). Potential immune escape mechanisms underlying the distinct clinical outcome of immune checkpoint blockades in small cell lung cancer. J. Hematol. Oncol. *12*, 67. https://doi.org/10.1186/s13045-019-0753-2.
38. Mauri, F., Schepkens, C., Lapouge, G., Drogat, B., Song, Y., Pastushenko, I., Rorive, S., Blondeau, J., Golstein, S., Bareche, Y., et al. (2021). NR2F2 controls malignant squamous cell carcinoma state by promoting stemness and invasion and repressing differentiation. Nat. Cancer *2*, 1152–1169. https://doi.org/10.1038/s43018-021-00287-5.
39. Tumeh, P.C., Harview, C.L., Yearley, J.H., Shintaku, I.P., Taylor, E.J.M., Robert, L., Chmielowski, B., Spasic, M., Henry, G., Ciobanu, V., et al. (2014). PD-1 blockade induces responses by inhibiting adaptive immune resistance. Nature *515*, 568–571. https://doi.org/10.1038/nature13954.
40. Zhang, J., Zhang, H., Zhang, L., Li, D., Qi, M., Zhang, L., Yu, H., Wang, D., Jiang, G., Wang, X., et al. (2022). Single-Cell Transcriptome Identifies Drug-Resistance Signature and Immunosuppressive Microenvironment in Metastatic Small Cell Lung Cancer. Adv. Genet. *3*, 2100060. https://doi.org/10.1002/ggn2.202100060.
41. Pan, X., Li, X., Dong, L., Liu, T., Zhang, M., Zhang, L., Zhang, X., Huang, L., Shi, W., Sun, H., et al. (2024). Tumour vasculature at single-cell resolution. Nature *632*, 429–436. https://doi.org/10.1038/s41586-024-07698-1.
42. Quail, D.F., and Joyce, J.A. (2013). Microenvironmental regulation of tumor progression and metastasis. Nat. Med. *19*, 1423–1437. https://doi.org/10.1038/nm.3394.
43. Zhang, H., AbdulJabbar, K., Moore, D.A., Akarca, A., Enfield, K.S.S., Jamal-Hanjani, M., Raza, S.E.A., Veeriah, S., Salgado, R., McGranahan, N., et al. (2023). Spatial Positioning of Immune Hotspots Reflects the Interplay between B and T Cells in Lung Squamous Cell Carcinoma. Cancer Res. *83*, 1410–1425. https://doi.org/10.1158/0008-5472.CAN-22-2589.
44. Xu, A.M., Haro, M., Walts, A.E., Hu, Y., John, J., Karlan, B.Y., Merchant, A., and Orsulic, S. (2024). Spatiotemporal architecture of immune cells and cancer-associated fibroblasts in high-grade serous ovarian carcinoma. Sci. Adv. *10*, eadk8805. https://doi.org/10.1126/sciadv.adk8805.
45. Fu, T., Dai, L.J., Wu, S.Y., Xiao, Y., Ma, D., Jiang, Y.Z., and Shao, Z.M. (2021). Spatial architecture of the immune microenvironment orchestrates tumor immunity and therapeutic response. J. Hematol. Oncol. *14*, 98. https://doi.org/10.1186/s13045-021-01103-4.
46. Enfield, K.S.S., Colliver, E., Lee, C., Magness, A., Moore, D.A., Sivakumar, M., Grigoriadis, K., Pich, O., Karasaki, T., Hobson, P.S., et al. (2024). Spatial Architecture of Myeloid and T Cells Orchestrates Immune Evasion and Clinical Outcome in Lung Cancer. Cancer Discov. *14*, 1018–1047. https://doi.org/10.1158/2159-8290.CD-23-1380.
47. Cheng, K., Li, X., Lv, W., Zhao, G., Zhou, R., Chang, C., Yang, H., Li, R., Li, Z., Chen, Y., et al. (2024). Spatial interactions of immune cells as potential predictors to efficacy of toripalimab plus chemotherapy in locally advanced or metastatic pancreatic ductal adenocarcinoma: a phase Ib/II trial. Signal Transduct. Target. Ther. *9*, 321. https://doi.org/10.1038/s41392-024-02031-8.
48. George, J., Lim, J.S., Jang, S.J., Cun, Y., Ozretić, L., Kong, G., Leenders, F., Lu, X., Fernández-Cuesta, L., Bosco, G., et al. (2015). Comprehensive genomic profiles of small cell lung cancer. Nature *524*, 47–53. https://doi.org/10.1038/nature14664.
49. Jiang, L., Huang, J., Higgs, B.W., Hu, Z., Xiao, Z., Yao, X., Conley, S., Zhong, H., Liu, Z., Brohawn, P., et al. (2016). Genomic Landscape Survey Identifies SRSF1 as a Key Oncodriver in Small Cell Lung Cancer. PLoS Genet. *12*, e1005895. https://doi.org/10.1371/journal.pgen.1005895.
50. Bankhead, P., Loughrey, M.B., Fernández, J.A., Dombrowski, Y., McArt, D.G., Dunne, P.D., McQuaid, S., Gray, R.T., Murray, L.J., Coleman, H.G., et al. (2017). QuPath: Open source software for digital pathology image analysis. Sci. Rep. *7*, 16878. https://doi.org/10.1038/s41598-017-17204-5.
51. Zhang, L., Yu, X., Zheng, L., Zhang, Y., Li, Y., Fang, Q., Gao, R., Kang, B., Zhang, Q., Huang, J.Y., et al. (2018). Lineage tracking reveals dynamic relationships of T cells in colorectal cancer. Nature *564*, 268–272. https://doi.org/10.1038/s41586-018-0694-x.
52. Yu, G., Wang, L.G., Han, Y., and He, Q.Y. (2012). clusterProfiler: an R package for comparing biological themes among gene clusters. OMICS *16*, 284–287. https://doi.org/10.1089/omi.2011.0118.
53. Karimi, E., Yu, M.W., Maritan, S.M., Perus, L.J.M., Rezanejad, M., Sorin, M., Dankner, M., Fallah, P., Doré, S., Zuo, D., et al. (2023). Single-cell spatial immune landscapes of primary and metastatic brain tumours. Nature *614*, 555–563. https://doi.org/10.1038/s41586-022-05680-3.

54. Jin, S., Guerrero-Juarez, C.F., Zhang, L., Chang, I., Ramos, R., Kuan, C.H., Myung, P., Plikus, M.V., and Nie, Q. (2021). Inference and analysis of cell-cell communication using CellChat. Nat. Commun. *12*, 1088. https://doi.org/10.1038/s41467-021-21246-9.

55. Garrido-Trigo, A., Corraliza, A.M., Veny, M., Dotti, I., Melón-Ardanaz, E., Rill, A., Crowell, H.L., Corbí, Á., Gudiño, V., Esteller, M., et al. (2024). Author Correction: Macrophage and neutrophil heterogeneity at single-cell spatial resolution in human inflammatory bowel disease. Nat. Commun. *15*, 857. https://doi.org/10.1038/s41467-024-45212-3.

56. Hu, C., Li, T., Xu, Y., Zhang, X., Li, F., Bai, J., Chen, J., Jiang, W., Yang, K., Ou, Q., et al. (2023). CellMarker 2.0: an updated database of manually curated cell markers in human/mouse and web tools based on scRNA-seq data. Nucleic Acids Res. *51*, D870–D876. https://doi.org/10.1093/nar/gkac947.

STAR★METHODS

KEY RESOURCES TABLE

REAGENT or RESOURCE	SOURCE	IDENTIFIER
Antibodies		
NR2F2 (clone EPR18443)	Abcam	Cat#ab211777; RRID: AB_2895604
FYN (clone EPR19636)	Abcam	Cat#ab184276; RRID: AB_2934009
SERPINA1 (clone AAT)	SANTA CRUZ	Cat#sc-59438; RRID: AB_781352
COL6A2 (clone EPR7889)	Abcam	Cat#ab180855; RRID: N/A
CD4 (clone EPR6855)	Abcam	Cat#ab133616; RRID: AB_2750883
CD8 (clone 4B11)	Invitrogen	Cat#MA1-80231; RRID: AB_929437
FOXP3 (clone D2W8E)	CST	Cat#98377; RRID: AB_2747370
CD20 (clone E7B7T)	CST	Cat#48750; RRID: AB_3107071
CD3D (clone EP4426)	Abcam	Cat#ab213362; RRID: AB_10859756
CD68 (clone KP1)	ZSGB-BIO	Cat#ZM-0060; RRID: AB_2904190
HIF1A (Polyclonal)	Proteintech	Cat#20960-1-AP; RRID: AB_10732601
DHRS2 (Polyclonal)	Invitrogen	Cat#PA5-25258; RRID: AB_2542758
ASCL1 (Polyclonal)	Abcam	Cat#ab74065; RRID: AB_1859937
NEUROD1 (clone 3H8)	Abcam	Cat#ab60704; RRID: AB_943491
POU2F3 (Polyclonal)	Bioss	Cat#bs-21046R; RRID: N/A
YAP1 (clone EP1674Y)	Abcam	Cat#ab52771; RRID: AB_2219141
Biological samples		
Patient derived primary tumors without lymph node metastasis	The Cancer Hospital, Chinese Academy of Medical Sciences (CHCAMS)	N/A
Patient derived primary tumors with lymph node metastasis	The Cancer Hospital, Chinese Academy of Medical Sciences (CHCAMS	N/A
Patient derived lymph node metastasized tumors	The Cancer Hospital, Chinese Academy of Medical Sciences (CHCAMS)	N/A
Critical commercial assays		
CosMx Universal Cell Characterization 1000-plex RNA Panel	Bruker Spatial Biology	Cat#121500041
Opal Polaris 7-Color Manual IHC Kit	AKOYA Biosciences	Cat#NEL861001KT
Deposited data		
SCLC CosMx SMI data	This paper	Zenodo: https://doi.org/10.5281/zenodo.15104582
SCLC single-cell RNA-seq data	Savchuk et al.[24]	GEO: GSE303152
SCLC bulk RNA-seq data	George et al.[48]	Table S10; https://doi.org/10.1038/nature14664
SCLC bulk RNA-seq data	Jiang et al.[49]	GEO: GSE60052
Software and algorithms		
R Statistical Software version v4.3.0	The R Foundation	https://www.r-project.org/
Seurat (v5.1.0)	CRAN Repository	https://cran.r-project.org/web/packages/Seurat/index.html
Harmony (v1.0)	CRAN Repository	https://cran.r-project.org/web/packages/harmony/index.html
QuPath (v0.5.1)	Bankhead et al.[50]	https://qupath.github.io/
Ro/e method	Zhang et al.[51]	https://doi.org/10.1038/s41586-018-0694-x
clusterProfiler (v4.8.3)	Yu et al.[52]	http://bioconductor.org/packages/release/bioc/html/clusterProfiler.html
Cell-cell pairwise interaction	Karimi et al.[53]	https://doi.org/10.1038/s41586-022-05680-3
CellChat (v1.6.1)	Jin et al.[54]	https://github.com/jinworks/CellChat.git

(*Continued on next page*)

Continued

REAGENT or RESOURCE	SOURCE	IDENTIFIER
ClusterR (v1.3.3)	CRAN Repository	https://cran.r-project.org/web/packages/ClusterR/index.html
GSVA (v2.0.7)	Bioconductor	https://new.bioconductor.org/packages/devel/bioc/html/GSVA.html
stats (v4.3.0)	CRAN Repository	https://search.r-project.org/R/refmans/stats/html/00Index.html
survminer (v0.4.9)	CRAN Repository	https://cran.r-project.org/web/packages/survminer/index.html
Survival (v3.4-0)	CRAN Repository	https://cran.r-project.org/web/packages/survival/index.html
BioRender	BioRender	https://www.biorender.com/
Other		
The spatial coordinate data, cell annotation information and analysis codes	This paper	https://github.com/ZhoulabCPH/SCLC-LNM-SMI.git

EXPERIMENTAL MODEL AND STUDY PARTICIPANT DETAILS

We retrospectively collected 105 archival formalin-fixed and paraffin-embedded (FFPE) tissue samples from 75 treatment-naïve SCLC patients who underwent surgical resection at the Cancer Hospital, Chinese Academy of Medical Sciences (CHCAMS) between January 2017 and December 2022. The cohort comprised three groups based on lymph node metastasis (LNM) status: 31 primary tumor samples from patients without LNM (PT group), 42 primary tumor samples from patients with concurrent LNM (PT-LNM group), and 32 matched lymph node metastasized tumor samples (LNMT group). The majority of patients presented with localized disease (limited stage according to VALSG criteria). Only one patient had multi-organ metastases (lung and pleura) confirmed intraoperatively and all other patients had no evidence of distant visceral metastases at the time of surgery. The study protocol was approved by the Ethics Committee and Institutional Review Boards of the Cancer Hospital, Chinese Academy of Medical Sciences (Approval No. 22/250–3452). The age, gender, stage, concurrent treatment and other clinical information of the SCLC patients was shown in Table S1. All procedures were performed in accordance with the ethical standards of the responsible committee and with the Helsinki Declaration. Informed consent was waived for this retrospective study using archival samples.

METHOD DETAILS

CosMx SMI data acquisition and processing

Spatial molecular imaging was conducted using the CosMx SMI platform (Bruker Spatial Biology) according to company manuals,[23] details are below.

Sample selection and preparation

FFPE blocks of primary and lymph node metastases were reviewed by two board-certified pathologists to confirm the diagnosis, and assess the quality of the tissue and tumor content. Representative tumor regions identified via H&E staining were selected to construct two tissue microarrays (TMAs). For TMA construction, 1 mm cores from each sample were arrayed into a recipient block. Serial 5 μm sections were cut from the TMA blocks and adhered onto VWR Superfrost Plus slides (VWR, 48311-703) for subsequent CosMx SMI analysis and H&E staining.

SMI library preparation and hybridization

The CosMx Human Universal Cell Characterization Panel (1000-plex RNA panel) was used for spatial transcriptomic profiling, strictly following the manufacturer's protocol (MAN-10184-02, Bruker Spatial Biology). The workflow included deparaffinization, target retrieval at 100°C for 15 min, protease digestion at 40°C for 30 min, overnight hybridization with the 1000-plex gene-specific probe panel, and serial rounds of fluorescent reporter hybridization, imaging, and cleavage (16 cycles) to decode all targets.

Morphological staining and imaging

Following RNA readout, the samples were stained with a five-fluorophore-conjugated antibody panel for cellular segmentation: DAPI (nuclei), PanCK (epithelium), CD45 (immune cells), CD68 (macrophages), and a cocktail of B2M/CD298 (membrane). z stack images (eight slices at 0.8 μm intervals) were acquired for each field of view (FOV, 260,100 μm^2) using the CosMx SMI instrument.

Image processing and cell segmentation

Raw image data were processed using the AtoMx Spatial Informatics Platform (v1.3).[23] Single-cell segmentation was performed using the "Cellpose" pretrained neural network model, which is the platform-standard and field-validated method optimized for

CosMx SMI data. This algorithm leverages the nuclear (DAPI), membrane (B2M/CD298), and protein morphology (PanCK, CD45 and CD68) signals to delineate cell boundaries. Transcripts were then assigned to cells based on their spatial coordinates relative to the segmented boundaries.

Data preprocessing and quality control

Following the quality control pipeline of CosMx SMI data described in a previous study,[55] cells with negative probe counts $\geq$1 or total detected genes (features) $\leq$ 20 were removed. Cells co-expressing high levels of both PanCK and CD45 protein (likely due to segmentation errors) were excluded. After quality control, 604,230 high-quality cells (81.5% of the total number of cells) were retained for downstream analysis. Gene expression counts were log-normalized (log1p) using Seurat (v5.1.0). Technical batch effects across samples were corrected using 'Harmony' (v1.0) applied to the top 50 principal components.

Multiplex immunofluorescence (mIF)

mIF was performed on serial FFPE sections using the Opal Polaris 7-Color Manual IHC Kit. Staining was performed using the Bond RX automated staining system, followed by imaging via the Vectra Polaris multispectral imaging system. The panel included antibodies against the following: NR2F2, FYN, HIF1A, SERPINA1, COL6A2, DHRS2, CD4, CD8, FOXP3, CD20, CD3D, and CD68. For antibody details, see the key resources table.

Immunohistochemistry (IHC)

IHC staining was performed on formalin-fixed, paraffin-embedded (FFPE) SCLC tissue sections using an automated BenchMark ULTRA stainer (Roche Diagnostics). Staining was conducted according to the manufacturer's protocol and validated internal laboratory standards. Primary antibodies and dilutions are as follows: ASCL1 (1:200, Abcam ab74065), NEUROD1 (1:150, Abcam ab60704), POU2F3 (1:300, Bioss bs-21046R), and YAP1 (1:80, Abcam ab52771). All stained slides were digitized using a KFBIO slide scanner (KF-PRO-400-HI) at 40$\times$ magnification. Protein expression was quantified in tumor regions by a certified pathologist using QuPath (v0.5.1).[50] An H-score was calculated for each marker by combining staining intensity and the percentage of positive tumor cells.

QUANTIFICATION AND STATISTICAL ANALYSIS

Dimensionality reduction and clustering

For the integrated CosMx SMI dataset, highly variable genes were identified using the FindVariableFeatures function in Seurat (v5.1.0). Principal component analysis (PCA) was performed using all 1,000 profiled genes. The top 50 principal components, which captured the majority of biological variance, were used for downstream analysis. A shared nearest neighbor graph was constructed using FindNeighbors, and unsupervised graph-based clustering was performed with FindClusters at a resolution of 0.8. For visualization, Uniform Manifold Approximation and Projection (UMAP) was applied to the Harmony-corrected principal components (dims = 1:20) using the RunUMAP function (umap.method = 'uwot'). This clustering process was repeated iteratively on subsets of cells to define finer subpopulations.

Cell type annotation

Putative marker genes for each cluster were identified using FindAllMarkers (only.pos = TRUE). Cell identities were assigned manually by cross-referencing these markers with canonical lineage-specific genes, the CellMarker 2.0 database,[56] and annotations from previous studies on SCLC.[3,15]

Tissue distribution preference

The enrichment or depletion of cell subsets across sample types was quantified using the ratio of observed to expected (Ro/e) calculation.[51] Statistical significance was assessed using a two-sided Fisher's exact test. A Ro/e value greater than 1 indicates significant enrichment in a given tissue context, while a Ro/e value between 0 and 0.2 indicates significant depletion.

Differential expression and functional analysis

Differentially expressed genes (DEGs) were identified using FindAllMarkers with a stringent threshold ($\log_2$FC > 1, adjusted p value <0.001, only.pos = TRUE). p-values were adjusted using the Benjamini-Hochberg (BH) method. Pathway and biological process enrichment analyses for Gene Ontology (GO) and Kyoto Encyclopedia of Genes and Genomes (KEGG) were conducted on DEG using the 'clusterProfiler' R package (v4.8.3).[52] Terms with a false discovery rate (FDR) of less than 0.05 were considered to be significantly enriched.

Cell-cell interaction/avoidance analysis

Pairwise spatial interactions were assessed using a permutation-based method.[53] Two cells were considered to be "interacting" if their centroids were within a 6 μm radius. For each sample, we calculated the observed frequency of interaction for every pairwise combination of cell types. To determine whether the observed frequency deviated significantly from a random spatial arrangement, we generated a null distribution through spatial permutation. For each of 1,000 permutations per sample, the *x* and *y* coordinates of all cells were randomized while preserving the overall cell density and sample boundaries. The p-value for an observed interaction

(or avoidance) frequency was calculated as the proportion of permutations where the randomized frequency was greater than or equal to (or less than or equal to, for avoidance) the observed frequency. *p*-values from individual samples within the same group were combined using Fisher's combined probability test. A combined *p*-value of less than 0.05 was considered statistically significant, indicating non-random spatial association (interaction) or dissociation (avoidance). The analysis assumed symmetry in pairwise relationships. Potential ligand-receptor interactions were inferred using the 'CellChat' R package (v1.6.1),[54] which models communication probability based on the expression of ligands and receptors and their published interaction databases. Significant ligand-receptor pairs were identified using a permutation test within the 'CellChat' framework ($p < 0.01$).

Cellular neighborhood (CN) identification

The local microenvironment for each cell was characterized by the cell-type composition of its 10 nearest neighbors. All of these local composition vectors were then aggregated and clustered using the MiniBatchKMeans function in the 'ClusterR' package (v1.3.3), with the batch_size parameter set to 100 and the initializer parameter set to 'kmeans++'. The optimal number of clusters (k) was determined by evaluating the average silhouette score across a range of k values and selecting the k that maximized this metric. The resulting clusters were defined as distinct CNs. To characterize each CN, we calculated the enrichment of specific cell types within it relative to their global abundance, using normalized odds ratios (OR). Statistical significance of enrichment was assessed via a two-sided Fisher's exact test, with *p*-values adjusted for multiple testing using the false discovery rate (FDR) method. An adjusted *p*-value of less than 0.05 was considered significant.

Public single-cell RNA-seq data processing

Processed single-cell RNA-seq data of primary SCLC tumors and brain, kidney, liver, and pleural metastases ($n = 24$ samples) from Savchuk et al.,[24] were downloaded from *Gene Expression Omnibus* (GEO, GSE303152). Data were re-processed using a standard 'Seurat pipeline' (v5.1.0) with consistent QC filters (500–10,000 genes, 1,000–60,000 UMIs, <10% mitochondrial gene content). Potential doublets were identified and removed using 'DoubletFinder' (v2.0.6) with an expected doublet rate of 2.5%. Data normalization was performed using NormalizeData, followed by the identification of the top 2,000 highly variable genes via FindVariableFeatures. PCA was conducted on the scaled data of these variable genes, and the top 50 principal components were used for downstream analysis. A shared nearest neighbor graph was constructed using FindNeighbors (dims = 1:10), and graph-based clustering was performed with FindClusters at a resolution of 0.5. For visualization, UMAP was applied using the top 30 principal components. To integrate data across multiple samples and mitigate the batch effects, we used Seurat's canonical correlation analysis (CCA) based integration workflow prior to the final clustering and visualization steps.

Public bulk RNA-seq data processing

Two independent published SCLC bulk RNA-seq cohorts were obtained from George's study[48] and Jiang's study.[49] Raw RNA-seq data from George cohort were processed and normalized to Fragments Per Kilobase Million (FPKM). The count expression profiles from the Jiang cohort were normalized using a $\log_2$ (count+1) transformation.

Survival analysis

To assess the association between CN abundance and patient survival, the patients were stratified into 'high' or 'low' groups for each CN, based on whether their sample level was above or below the median value across the entire cohort. To validate the spatial gene signature, the top 20 DEGs defining the prognostically favorable Pan-immune hotspot-1 (PIHs-1) were used to create a gene signature. A single-sample gene set enrichment analysis (ssGSEA) score for this signature was computed for each sample in the independent bulk RNA-seq cohorts using the 'GSVA' package (v2.0.7). The cohorts were dichotomized into PIHs-1 high/low groups based on the median ssGSEA score for survival analysis. Survival differences were evaluated using the Kaplan-Meier method and the log rank test. Univariable and multivariable Cox proportional hazards models were constructed using the 'survival' R package (v3.5-7). Hazard ratios (HR) and 95% confidence intervals (CI) are reported.

Statistical analysis

All statistical analyses and data visualizations were conducted in R (v4.3.0). Unless otherwise specified, comparisons between two groups were performed using two-sided Wilcoxon rank-sum tests. Correlations were assessed using Spearman's rank correlation coefficient. All tests were two-sided, and a *p* value of less than 0.05 was considered significant; ns denotes not significant ($p > 0.05$).